

Self-Assembly of Nanoparticle-Spiked Pillar Arrays for Plasmonic Biosensing

Sung-Gyu Park,* Xiaofei Xiao, Jouha Min, ChaeWon Mun, Ho Sang Jung, Vincenzo Giannini, Ralph Weissleder, Stefan A. Maier, Hyungsoon Im,* and Dong-Ho Kim*

Plasmonic biosensors have demonstrated superior performance in detecting various biomolecules with high sensitivity through simple assays. Scaled-up, reproducible chip production with a high density of hotspots in a large area has been technically challenging, limiting the commercialization and clinical translation of these biosensors. A new fabrication method for 3D plasmonic nanostructures with a high density, large volume of hotspots and therefore inherently improved detection capabilities is developed. Specifically, Au nanoparticle-spiked Au nanopillar arrays are prepared by utilizing enhanced surface diffusion of adsorbed Au atoms on a slippery Au nanopillar arrays through a simple vacuum process. This process enables the direct formation of a high density of spherical Au nanoparticles on the 1 nm-thick dielectric coated Au nanopillar arrays without high-temperature annealing, which results in multiple plasmonic coupling, and thereby large effective volume of hotspots in 3D spaces. The plasmonic nanostructures show signal enhancements over 8.3×10^8 -fold for surface-enhanced Raman spectroscopy and over 2.7×10^2 -fold for plasmon-enhanced fluorescence. The 3D plasmonic chip is used to detect avian influenza-associated antibodies at 100 times higher sensitivity compared with unstructured Au substrates for plasmon-enhanced fluorescence detection. Such a simple and scalable fabrication of highly sensitive 3D plasmonic nanostructures provides new opportunities to broaden plasmon-enhanced sensing applications.

so-called “plasmonic hotspots” are the fundamental basis of numerous promising technologies in the fields of plasmon-enhanced spectroscopy,^[1–10] plasmonic biosensing,^[11–14] photocatalysis,^[15–19] and nanophotonics.^[20,21] One major challenge in expanding the use of plasmon-enhanced applications lies in reproducible fabrication of high-density plasmonic hotspots over large areas in a low-cost, high-throughput manner. Various methods have been explored, including aggregations of metallic nanoparticles, nanolithographic patterning, thin-film processing, and hybrid nanostructures. Despite extensive efforts, the development of a reproducible, commercially ready fabrication method that achieves both high quality (i.e., high sensitivity and good reproducibility) and high throughput (i.e., low-cost and wafer-scale fabrication) remains elusive.

Among various plasmonic configurations, a nanoparticle-on-mirror (NPOM) geometry, where a nanoparticle is separated from a plain metal film by an ultrathin dielectric spacer layer, has been reported to be a highly efficient plasmonic substrate.^[1–5] In the 2D NPOM configuration, however, electromagnetic hotspots are formed around the nanoparticle in a limited area; the effective hotspot volume accounts for a small fraction of the total

1. Introduction

Strongly enhanced electromagnetic fields localized at interstitial nanogap junctions between metallic nanostructures,

reported to be a highly efficient plasmonic substrate.^[1–5] In the 2D NPOM configuration, however, electromagnetic hotspots are formed around the nanoparticle in a limited area; the effective hotspot volume accounts for a small fraction of the total

Dr. S.-G. Park, C. W. Mun, Dr. H. S. Jung, Dr. D.-H. Kim
Advanced Nano-Surface Department
Korea Institute of Materials Science (KIMS)
Changwon, Gyeongnam 51508, Korea
E-mail: sgpark@kims.re.kr; dhkim2@kims.re.kr

X. Xiao, Dr. V. Giannini, Prof. S. A. Maier
The Blackett Laboratory Department of Physics
Imperial College London
London SW7 2AZ, UK

Dr. J. Min, Prof. R. Weissleder, Prof. H. Im
Center for Systems Biology (CSB)
Massachusetts General Hospital
Boston, MA 02114, USA
E-mail: im.hyungsoon@mgh.harvard.edu

 The ORCID identification number(s) for the author(s) of this article can be found under <https://doi.org/10.1002/adfm.201904257>.

Dr. V. Giannini
Instituto de Estructura de la Materia (IEM)
Consejo Superior de Investigaciones Científicas (CSIC)
Serrano 121, Madrid 28006, Spain

Prof. R. Weissleder, Prof. H. Im
Department of Radiology
Massachusetts General Hospital
Boston, MA 02114, USA

Prof. R. Weissleder
Department of Systems Biology
Harvard Medical School
Boston, MA 02115, USA

Prof. S. A. Maier
Nano-institut München
Fakultät für Physik
Ludwig-Maximilians-Universität München
80539 München, Germany

DOI: 10.1002/adfm.201904257

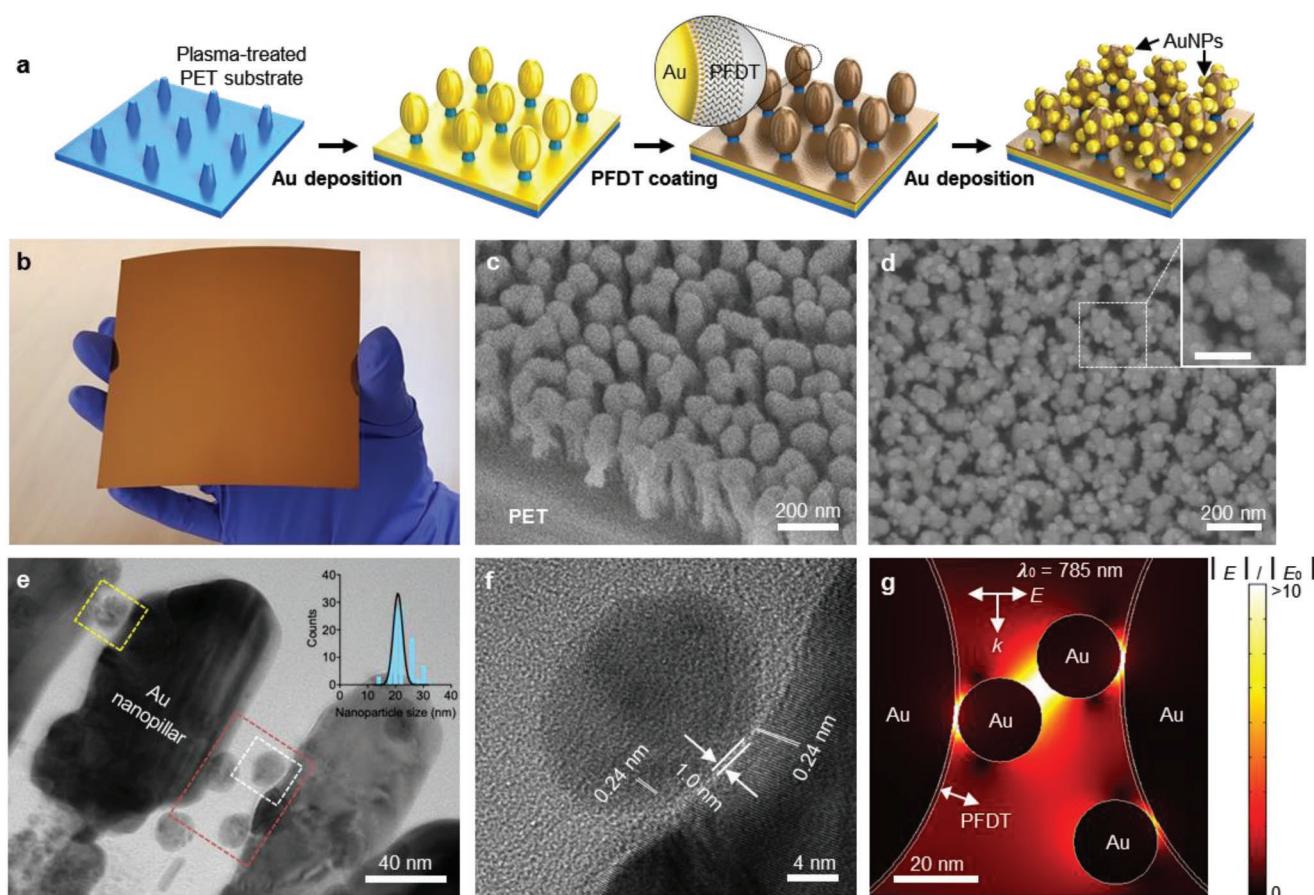


Figure 1. Fabrication of Au nanoparticles (AuNPs) on Au nanopillars (NPOP) structures. a) Schematic of the fabrication procedure. Au deposition onto an Ar-plasma-etched PET substrate produces Au nanopillars. After vapor deposition of 1*H*, 1*H*, 2*H*, 2*H*-perfluorodecanethiol (PFDT), a second Au deposition forms nanoparticles on the PFDT-coated nanopillars. b) Photograph of wafer-scale (90 cm² area) chip fabrication. Scanning electron images of c) nanopillars formed on a PET substrate and d) 3D NPOP structures formed by deposition of 20 nm of Au onto the PFDT-coated nanopillars. The inset in (d) is a zoomed-in image of the region of the 3D NPOP indicated by a dashed box. The scale bar in the inset is 100 nm. e) Transmission electron image of 3D NPOP structures. The inset in (e) shows the size distribution of AuNPs on the nanopillars. f) High-resolution transmission electron image showing a zoomed-in image of the white dashed box in (e). The thickness of the PFDT layer between the AuNP and nanopillar is ≈1 nm. g) Finite element method (FEM) simulation of the 3D NPOP structure shown in the red dashed box in inset (e).

volume of the structure. The 2D NPOM system also requires high-precision side-illumination optics to achieve maximum plasmonic coupling at the glancing incidence angle of light;^[1,4] this requirement increases the optical complexity and limits the use of low-cost spectroscopy systems. Therefore, for broader and translational applications, it is important to expand 2D plane mirrors into 3D nanostructures that can readily excite efficient plasmonic coupling between plasmonic nanostructures in 3D spaces.^[22–25]

Here, we present new 3D plasmonic nanostructures composed of spherical Au nanoparticles (AuNPs) on 3D Au nanopillars (NPOP) with a 1 nm-thick uniform spacer layer between the AuNPs and the nanopillars. The method is based on enhanced surface diffusion of adsorbed Au atoms (i.e., adatoms) on a low-energy surface; the Au adatoms diffuse into defective sites of the underlying film and form clustered atoms (i.e., AuNPs). This process enables the direct and selective formation of spherical Au nanoparticles through a simple Au deposition process without high-temperature annealing. The AuNPs density can be highly increased by introducing more

nucleation sites on the 3D rough Au nanopillar surface. The 3D NPOP structures provide high-density hotspots and large effective volumes of molecular binding sites for highly sensitive surface-enhanced Raman spectroscopy (SERS) and plasmon-enhanced fluorescence (PEF). We demonstrate highly improved detection sensitivities for both SERS and PEF sensing applications. The fabrication method developed here is cheap, simple, reproducible, and applicable to scaled-up chip production.

2. Results and Discussion

2.1. Fabrication of 3D NPOP Nanostructures

Figure 1a shows a schematic of the fabrication procedure for the 3D NPOP substrates. First, a polyethylene terephthalate (PET) substrate was etched with Ar plasma to form polymer nanopillars. A 100 nm-thick Au film was deposited onto the nanopillars by either conventional sputtering or thermal evaporation to form high-density Au-coated nanopillars.^[23] As a space layer, a

self-assembled monolayer (SAM) of 1*H*,1*H*,2*H*,2*H*-perfluorodecanethiol (PFDT) was vapor-deposited onto the Au nanopillars. Finally, another layer of Au was deposited onto the PFDT-coated Au nanopillars. We chose PFDT as a spacer layer because of its low surface energy ($\gamma_{\text{PFDT}} = 0.015 \text{ J m}^{-2}$), which is two orders of magnitude lower than that of Au ($\gamma_{\text{Au}} = 1.54 \text{ J m}^{-2}$).^[26] This low surface energy was experimentally confirmed by contact angle measurements (Figure S1, Supporting Information). Because of the large difference in surface energy between the PFDT layer and Au, the Au adatoms on the PFDT surface diffuse until they form spherical AuNPs rather than forming a continuous layer, resulting in the Au 3D NPOP structures. This fabrication method is simple, fast, and scalable to the wafer scale with high reproducibility (Figure 1b). Scanning electron microscopy (SEM) revealed the formation of high-density Au pillars (Figure 1c) and AuNPs on the surface of the PFDT-coated nanopillars (Figure 1d). Interestingly, spherical AuNPs were preferentially self-assembled around the top edges of the PFDT-coated nanopillars (inset in Figure 1d). Transmission electron microscopy (TEM) provided a high-resolution image of the AuNPs formed on the Au nanopillars (Figure 1e). With the deposition of a 20 nm-thick Au layer, the mean diameter of the AuNPs was 22.5 nm with a uniform size distribution of 3.7 nm in the standard deviation (inset in Figure 1e). The high-resolution TEM image in Figure 1f shows a 1 nm uniform gap created by the PFDT layer between a AuNP and a nanopillar. The image also shows lattice fringes with an interplanar space of 0.24 nm, corresponding to the (111) plane of the Au face-centered cubic structure.^[27] This result demonstrates the crystalline nature of the AuNPs and Au nanopillars. Depending on the distance between nanopillars, the AuNPs generate hotspots at nanogap junctions between AuNPs or bridged between nanopillars (red and yellow dashed box in Figure 1e). We investigated the near-field coupling of these structures using computational finite-element simulations (Figure 1g; Figure S2, Supporting Information). The simulations clearly show that the 3D NPOP structures generate multiple hotspots localized at junctions between AuNPs and nanopillars as well as at the nanogap between AuNPs, due to localized surface plasmon resonance (LSPR) coupling effects.^[9] High-field enhancements were achieved at both 633 and 785 nm by normally incident plane-wave illumination. In both wavelengths, the ellipsoidal shapes of nanopillars facing upward and AuNPs deposited onto the sidewalls of the nanopillars enable more efficient plasmon coupling from normally incident light compared with the plasmon coupling achieved with 2D NPOM structures.^[24]

2.2. Mechanism of Surface-Diffusion-Mediated AuNP Formation

Surface free energy is a key to understanding the atomic behavior of adatoms on the surface. Atoms lie on the surface and control the formation of atomic clusters (i.e., nuclei), which leads to the growth of NPs during the vacuum deposition process.^[28] The surface energy of a PFDT monolayer is approximately 100 times lower than that of Au adatoms; consequently, the Au adatoms on the PFDT surface diffuse and form atomic clusters at defective sites—so-called nucleation (Figure 2a). The nucleation sites are predominantly formed

at defective surface areas (e.g., grain boundaries), where the binding energy of adatoms is greater than that of adatoms on a planar surface because of the lower density of the PFDT layer at the defective sites.^[29] Figure 2b shows a 100 nm-thick plain Au film deposited onto a Si wafer, where grain boundaries can be identified. An atomic force microscopy (AFM) image visualizes the grain boundaries concave from the top surface (Figure S3a, Supporting Information). After vapor-phase deposition of PFDT, 10 nm-thick Au was deposited onto the PFDT-coated plain Au substrate by thermal evaporation, resulting in AuNP formation (Figure 2c; Figure S3b, Supporting Information). Here, AuNPs are observed to have formed only at the grain boundaries rather than on the smooth facets. In addition, some triangular-shaped AuNPs formed at triple grain junctions (dotted circles in Figure 2c). These observations support the hypothesis that Au adatoms diffuse to grain boundaries and form AuNPs selectively at the recessed grain-boundary regions through nucleation, which is a basic principle of AuNP formation via vacuum deposition process.

The same mechanism of AuNP formation can be applied to 3D nanopillars (Figure 2d). Au deposition onto the PFDT-coated nanopillars produce spherical-shaped AuNPs, consistent with predictions based on Volmer–Weber growth mode.^[30,31] Because the tops of the nanopillars exhibit a large curvature, AuNPs are preferentially formed around the top edges or on the sidewalls of the nanopillars (Figures 1e and 2e). The surface diffusion-mediated NPs formation can also be applied to other metals. We demonstrated silver nanoparticles (AgNPs) formation on PFDT-coated Au nanopillars (Figure 2f; Figure S4, Supporting Information). However, the overall hotspot densities were lower than those with AuNPs. When the film thickness was increased to 80 nm, most of the AgNPs were merged together (Figure S4, Supporting Information), whereas the AuNPs were still spaced apart at a film thickness of 100 nm (Figure S5, Supporting Information). These results are attributable to a lower surface energy of Ag ($\gamma_{\text{Ag}} = 1.20 \text{ J m}^{-2}$) compared with that of Au ($\gamma_{\text{Au}} = 1.54 \text{ J m}^{-2}$).^[32] Finally, we tested alumina (Al_2O_3), which has a high surface energy ($\gamma_{\text{alumina}} = 0.97 \text{ J m}^{-2}$), as a spacer layer.^[33] As shown in Figure S6 (Supporting Information), AuNPs did not form on the alumina-coated nanopillars, further confirming the importance of a low surface energy of the underlying dielectric layer for spherical AuNPs formation.

2.3. Thickness Optimization

Next, we tested different Au deposition thicknesses for AuNPs formation and characterized the optical properties of the deposited films. The Au also exhibits much greater chemical stability and biocompatibility than the Ag; we therefore used 3D Au NPOP substrates in subsequent sensing experiments. As we increased the Au deposition thickness from 20 to 80 nm on the PFDT-coated rough nanopillars, the size of the AuNPs gradually increased (Figure 3a,b; Figure S7, Supporting Information). We previously demonstrated that the surface roughness of the nanopillars can be increased by depositing the Au by thermal evaporation rather than by Au sputtering.^[25] The thermal evaporation process creates nanoscale asperities on the

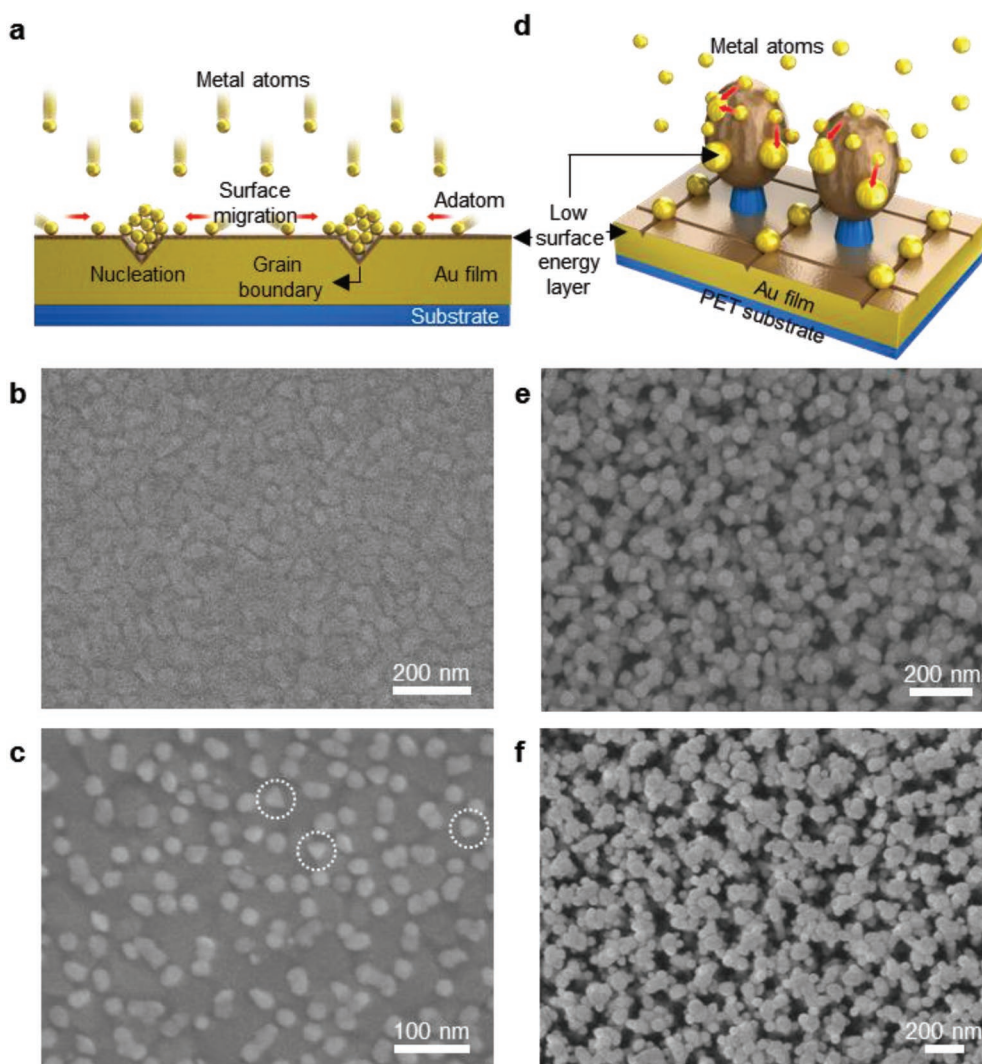


Figure 2. Surface-diffusion-induced AuNP formation from vacuum deposition. a) A schematic showing the selective nucleation of Au adatoms at grain boundaries. Scanning electron images of a PFDT-treated 2D plain Au substrate b) before and c) after Au deposition. The AuNPs were formed via self-nucleation at grain boundaries. White dotted circles indicate triangular-shaped nanoparticles formed at triple grain junctions. d) A schematic showing AuNP formation on 3D smooth nanopillars. Scanning electron images of 3D e) Au NPOP and f) Ag NPOP substrates. On top of the PFDT-coated Au nanopillars, e) 40 nm of Au or f) 40 nm of Ag was deposited to form NPs on the nanopillar surface via self-nucleation and growth of deposited metal atoms. Au and Ag NPs are preferentially self-assembled around the top edges of smooth Au nanopillars.

Au nanopillars, which increase the surface roughness (average roughness $R_{\text{evaporation}} = 20.03$ nm; Figure S8, Supporting Information) to approximately twice that of a sputtered Au film ($R_{\text{sputter}} = 11.30$ nm; Figure S3a, Supporting Information). With the deposition of a 20 nm-thick Au layer, AuNPs were compactly covered the entire top surface and sidewalls of the PFDT-coated Au nanopillars (Figure S7a, Supporting Information). Even when the deposition thickness reached 100 nm, the AuNPs were still spaced apart and exhibited a mean diameter of 70 nm, resulting in multiple nanogaps-enhanced plasmonic coupling effects (Figure S7b,c, Supporting Information). The population density of the AuNPs gradually decreased from $750 \mu\text{m}^{-2}$ (20 nm Au deposition) to $325 \mu\text{m}^{-2}$ (100 nm deposition) for rough nanopillars (Figure 3c). It can be concluded that the AuNPs density can be highly increased by introducing more nucleation sites on the 3D rough Au nanopillar surface.

Figure 3d shows transmission spectra of the 3D Au NPOP structures prepared with different thicknesses of deposited Au on the smooth nanopillars. The underlying 3D Au nanopillars have a distinct LSPR peak at 518 nm and this peak red-shifts to 520 nm when a PFDT coating is applied to the nanopillars. When AuNPs are formed on the PFDT-treated Au nanopillars, light transmittance at wavelengths greater than 600 nm rapidly decreases because of multiple plasmonic coupling effects of 3D NPOP structures at these wavelengths (inset in Figure 3e; Figure S9, Supporting Information). With the formation of larger AuNPs, the transmittance of the 3D NPOP structures converges to zero. The average transmittance of the 3D NPOP structures in the visible wavelength range (400–800 nm) decreased to less than 0.1% (Figure 3e), which indicates that almost no visible light is transmitted through the 3D plasmonic nanostructures. The corresponding extinction spectra of the 3D NPOP array

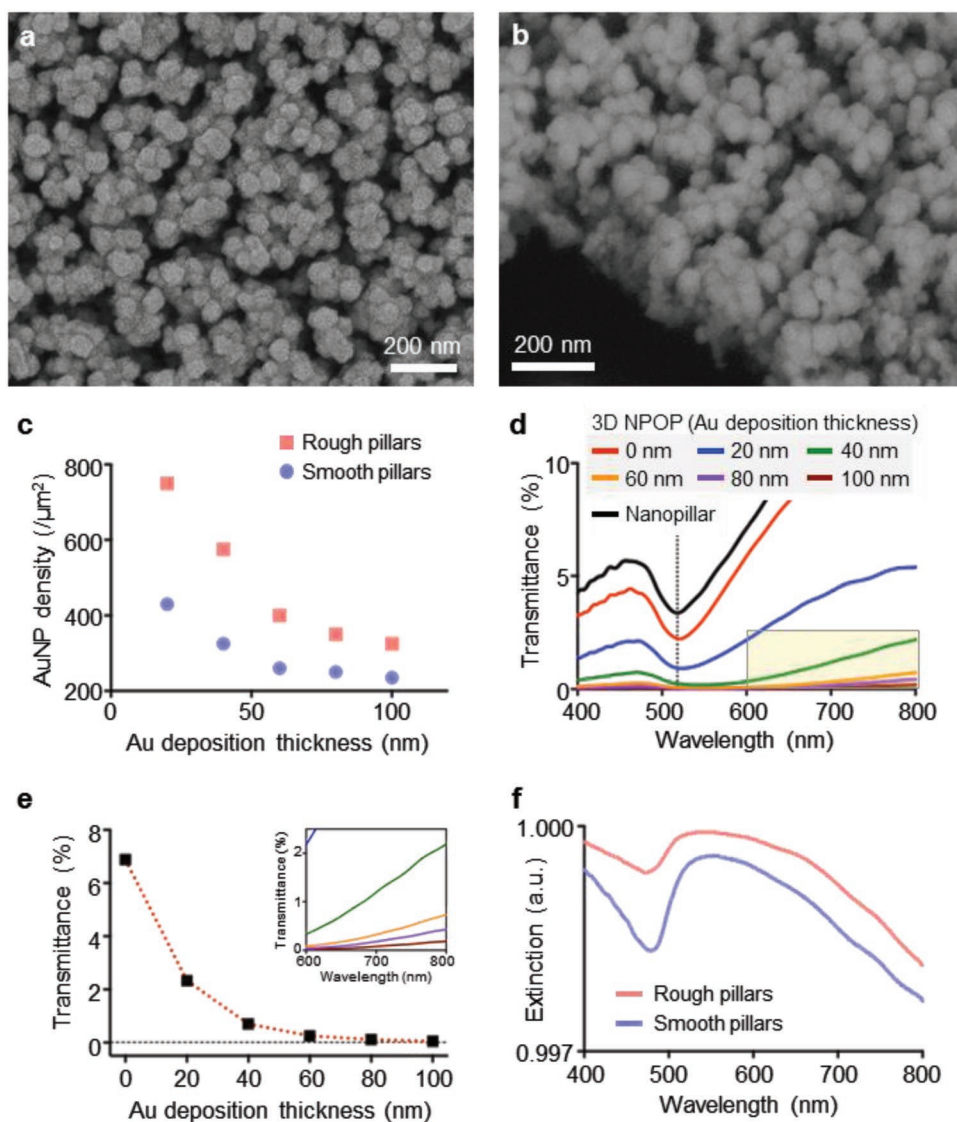


Figure 3. Optimization with 3D Au NPOP structures with various Au deposition thicknesses. a,b) Scanning electron images of 3D Au NPOP structures made by 80 nm Au deposition on PFDT-treated rough Au nanopillars. c) Densities of upper AuNPs formed after deposition of various thicknesses of Au onto rough (prepared by evaporation) or smooth (prepared by sputtering) nanopillars. d) Transmission spectra of the underlying nanopillar and the 3D Au NPOP structures prepared with various thicknesses of Au on PFDT-treated smooth nanopillars. The dashed line indicates the distinct localized surface plasmon resonance (LSPR) peak (518 nm) of the Au-nanopillar substrate. e) Average light transmittance of 3D Au NPOP structures in visible wavelengths ranging from 400 to 800 nm. f) Extinction spectra of Au NPOP structures prepared by deposition of 80 nm of Au onto rough or smooth nanopillars.

are acquired directly from the transmittance (T) and plotted as $(1 - T)$.^[34,35] Enhanced light–matter interactions between plasmonic nanostructures result in high extinction values across the entire visible wavelength range (Figure 3f). The 3D NPOP structure prepared on rough nanopillars shows higher extinction values than the structure on smooth nanopillars, predominantly because of the higher surface coverage of AuNPs and thereby enhanced light–matter interactions on the 3D rough surface.

2.4. Surface-Enhanced Raman Spectroscopy

A substrate with a high density of plasmonic nanostructures formed in 3D spaces is highly desirable for SERS and PEF.

We first investigated the SERS performance of the 3D NPOP substrates using an organic dye, methylene blue (MB). A 3 μL solution of 5×10^{-6} M MB was applied to the surface of the 3D NPOP substrates, and the solvent was allowed to evaporate. The SERS signal was measured with a handheld Raman spectrometer at an excitation wavelength of 785 nm (Figure 4a,b). The 3D NPOP substrates prepared with deposition of 80 nm-thick Au on the rough Au nanopillars exhibited the most intense SERS signal, which was about 200 times greater than the signal (at 1625 cm^{-1} , blue dashed line in Figure 4a,b) of the Au nanopillars (Figure 4c). We previously reported that single-layer Au nanopillars show an averaged SERS enhancement factor (EF) on the order of 10^6 .^[25] The formation of AuNPs via metal deposition results in additional 200-fold SERS signal enhancement.

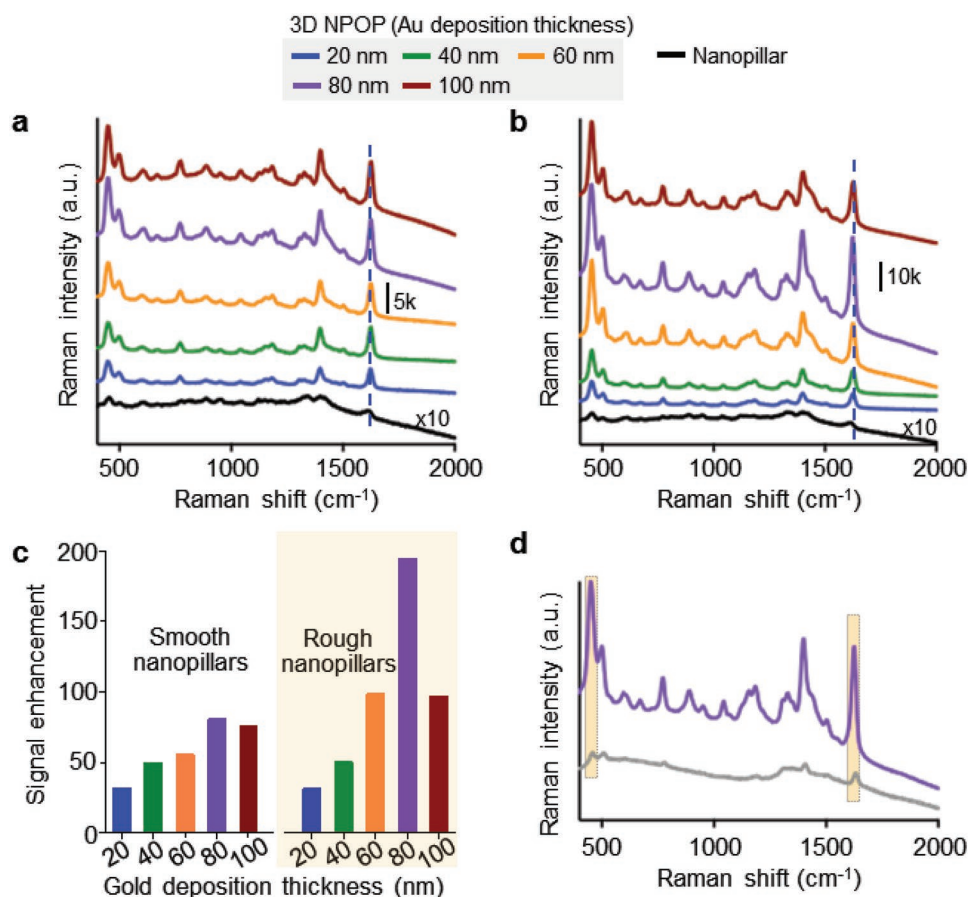


Figure 4. Surface-enhanced Raman spectroscopy (SERS) characterization of 3D NPOP structures. SERS signals of 5×10^{-6} M methylene blue on 3D Au NPOP structures made with Au deposition at various thicknesses onto a) smooth or b) rough Au nanopillars. c) SERS signal enhancements of Au NPOP structures made with Au deposition at various thicknesses, normalized by the SERS signal of single layer Au nanopillars. d) Raman signal comparison between an Au NPOP structure made with 80 nm Au deposition on rough nanopillars and a neat Raman measurement for SERS enhancement factor calculation. The concentrations of methylene blue were 1.5×10^{-15} mol for the Au NPOP substrate and 6.0×10^{-10} mol for the Raman measurement. The integration times were 0.1 s for the Au NPOP substrate and 30 s for the Raman measurement.

Overall, rough nanopillars showed signals twice as intense as those of smooth nanopillars at the same thickness because of their higher hotspots densities (Figure 3c). In our measurements, the optimized 3D NPOP substrate showed a SERS EF of 8.3×10^8 at 420 cm^{-1} and 4.3×10^8 at 1625 cm^{-1} , respectively (yellow shaded region in Figure 4d). Equally as important as the high SERS EF, the 3D NPOP substrates exhibit high signal uniformity, with a coefficient of variation for SERS signals of $<5.8\%$ for 36 measurements in a 90 cm^2 area (Figure S10, Supporting Information).

2.5. Plasmon-Enhanced Fluorescence Biosensing

Another potential application of the 3D NPOP structure is detecting target molecules using PEF. Similar to SERS, fluorescence signals are amplified when fluorophores are located at plasmonic hotspots.^[36] As proof-of-concept, we used the 3D Au NPOP chips to detect avian influenza (AI)-associated antibodies.^[37] Controlling avian influenza requires not only sensitive field testing but also global surveillance because of its

fast spread. Therefore, the ability to produce a large number of sensitive chips at low cost is critical. For fluorescence measurements, we used the 3D Au NPOP chip prepared with an 80 nm-thick Au layer. We chose the substrate based on thickness optimization done by SERS characterization (Figure 4a–c); the substrate with 80 nm-thick Au showed the highest SERS signal enhancement. The maximum signal enhancement factors in terms of fluorescence intensity and hotspot count after background correction were measured as 2.7×10^2 and 3.4×10^2 , respectively (Figure S11, Supporting Information). The enhancement factor may vary depending on the concentration of target molecules compared to hot spot densities. We next compared the detection sensitivity of the 3D Au NPOP with that of plain Au substrates using titrating concentrations of target antibodies against influenza hemagglutinin (HA) as a model system. The 3D NPOP or plain Au substrates were coated with HA peptides to capture the influenza-associated HA-antibodies (HA-Abs), followed by labeling with secondary antibodies conjugated with Alexa Fluor 647 for PEF detection. We chose Alex Fluor 647 because of its spectral overlap with the wavelength that achieves high electric field enhancements

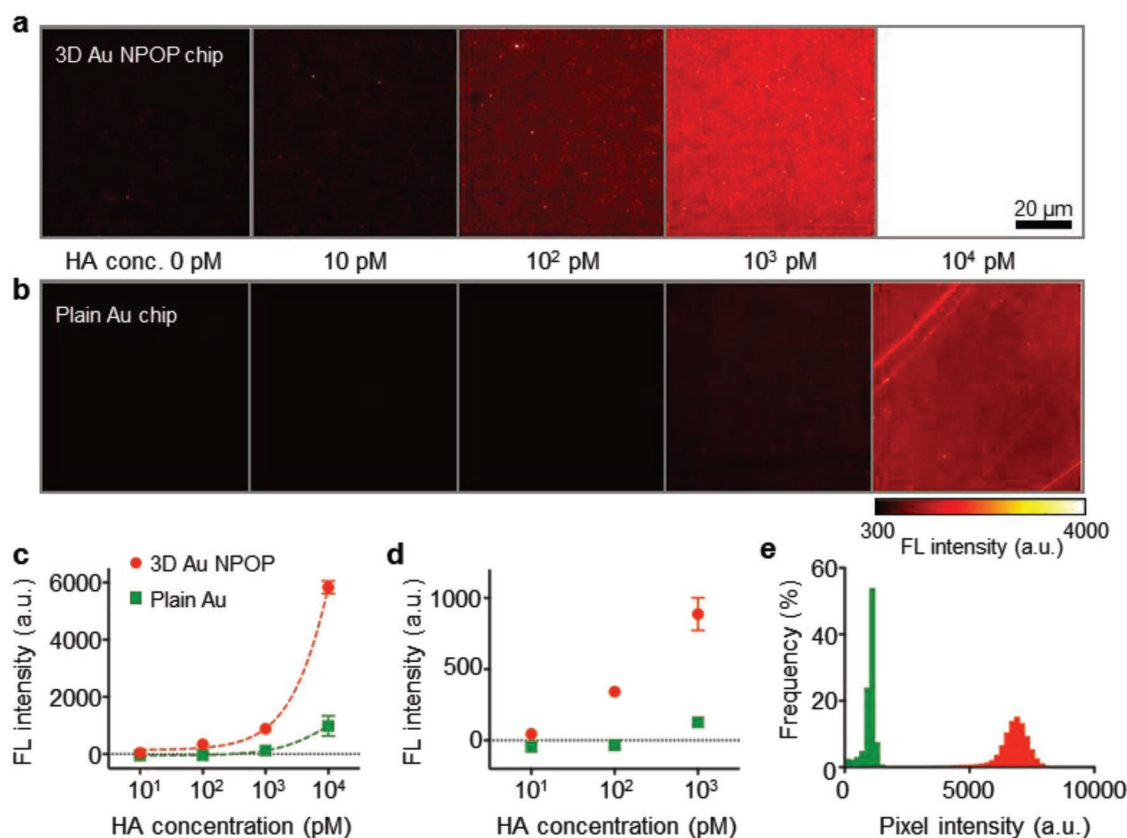


Figure 5. Detection of avian influenza-associated antibody. Different concentration of anti-hemagglutinin antibodies (HA-Abs) were fluorescently detected on a) 3D Au NPOP chips and b) plain Au substrates. The Au substrates were coated with HA tag peptides to capture the HA-Abs, which were labeled by secondary antibodies conjugated with Alexa Fluor 647. c) Comparison of the mean fluorescence intensities between the Au chip and plain substrate. The fluorescence intensity was normalized by background signals defined by the sum of the mean fluorescence intensity in the absence of target HA-Abs and three times the standard deviation. d) The limit of detection of the Au NPOP chip is ≈ 100 times greater (10×10^{-12} M) than that of the plain Au substrate (1×10^{-9} M). e) Histograms of pixel intensities between the Au chip and the plain Au substrate in the detection of 10×10^{-9} M HA-Abs.

(Figure 3f). Titration experiments with different concentrations of HA-Abs indicated that the 3D NPOP chips provide a highly enhanced fluorescence signal of Alex Fluor 647 dyes and are more sensitive than the plain Au substrates for detecting the HA-Abs (Figure 5a,b). The limit of detection (LOD) was estimated using a standard formula: the HA-Abs concentration that generated an analytical signal equal to three times the standard deviation of the signals of blank samples as a negative control. From the titration experiments, we established a LOD of 10×10^{-12} M for the 3D Au NPOP chip; similar measurements with the plain Au substrate required more than 1×10^{-9} M for reliable detection (Figure 5c,d). The histogram graphs of pixel intensities in the detection of 10×10^{-9} M HA-Abs also confirm that the 3D Au NPOP chip provides stronger signals than the plain Au substrate (Figure 5e).

3. Conclusions

In summary, we presented new 3D plasmonic nanostructures having spherical plasmonic nanoparticles on the Au nanopillars with a 1 nm-thick uniform dielectric spacer layer. The high-density Au nanoparticles are directly formed and self-assembled on the 3D nanopillar arrays during a vacuum deposition

process. The method is based on enhanced surface diffusion of adsorbed atoms, and selective nucleation and growth on the 3D plasmonic surface with low surface energy. High sensitivity and reproducibility make the 3D plasmonic substrates an ideal bioanalytical platform for single-molecular detection assays. Combined with the advantage of high-throughput and wafer-scale chip production, the new approach will accelerate clinical translation of plasmon-enhanced sensing methods and will be applicable for detecting other biomolecules (Figure S12, Supporting Information) such as proteins, RNA, DNA, and extracellular vesicles.

4. Experimental Section

Fabrication of 3D NPOP Substrates: A PET polymer substrate with a thickness of 188 μm , purchased from Toray, was used after removal of its protective film. The polymer substrate was treated with Ar plasma using a custom-built 13.56 MHz RF ion-etching instrument (LAT, Korea). The inlet Ar flow rate and the working pressure were fixed at five standard cubic centimeters per minute (sccm) and 80 mTorr, respectively, during the Ar plasma treatment, which was conducted for 2 min. The plasma power was 100 W. A 100 nm-thick Au layer was directly deposited onto the PET nanopillars at a deposition rate of 2.0 \AA s^{-1} using a sputtering or thermal evaporation system (LAT, Korea). The base pressure of

the chamber was 9.6×10^{-6} Torr. The as-prepared Au/PET nanopillar substrates were then treated with PFDT. A 97% PFDT solution was purchased from Sigma-Aldrich (St. Louis, MO, USA). Specifically, 10 μL of a 97% PFDT solution was poured into a glass Petri dish, and the lid of the Petri dish was closed for 2 h. The lid was attached to the Au/PET substrate. Finally, Au was thermally evaporated onto the PFDT-treated Au/PET nanopillar substrate at a deposition rate of 0.3 \AA s^{-1} using thermal evaporation process (LAT, Korea). The deposition rate was monitored by a quartz crystal microbalance.

Characterization: UV-vis transmission spectra were recorded with a Cary 5000 spectrophotometer (Agilent, USA). Transmittance values were normalized to air. Water contact angles were measured using contact-angle goniometry (FEMTOFAB, SCLab-200TEZ). The surface morphologies were characterized by field-emission scanning electron microscopy (FE-SEM; Jeol JSM-6700F). The Au NP population densities were estimated by SEM images. From top-view of each image, we manually counted the formed Au NPs in $1 \times 1 \mu\text{m}^2$ areas. The SERS spectra were recorded using a handheld Raman spectrometer (CBEx, Snowy Range Instruments) with a 785 nm laser; the laser power was 10 mW.

Plasmon-Enhanced Fluorescence Measurement: The 3D Au NPOP chips or plain Au chips were cleaned in ethanol and acetone with sonication for 15 min. 11-Mercaptoundecanoic ($10 \times 10^{-3} \text{ M}$ in EtOH, Sigma-Aldrich) was added onto the chips for overnight incubation. After being washed three times with MES buffer (2-(*N*-morpholino)ethanesulfonic acid, pH 5, Thermo Fisher), the chips were incubated for 10 min at room temperature in a solution of 1-ethyl-3-(3-dimethylaminopropyl) carbodiimide (EDC, final concentration of 0.2 M, Thermo Fisher) and sulfo-*N*-hydroxysulfosuccinimide (sulfo-NHS, final concentration of 0.5 M, Thermo Fisher) in MES buffer. The chips were washed three times in MES buffer, and then hemagglutinin (HA)-tag peptides (10 mg mL^{-1} in MES, CS Bio Co.) was added for 1 h incubation at room temperature. The chip surfaces were then blocked in a Superblock solution (Thermo Fisher) for 15 min. A serial dilution standard (anti-HA antibodies, Abcam) in 0.2% bovine serum albumin (BSA) in phosphate-buffered saline (PBS) solution were added to each chip for 30 min of incubation at room temperature. Unbound antibodies were washed with a PBS solution with 0.05% Tween-20 three times. Anti-mouse IgG-Alexa Fluor 647 (1:200, diluted in 0.2% BSA-PBS solution) were added on the chips for 15 min at room temperature. After being washed with PBS, the chips were imaged with a fluorescence microscope (Olympus BX63).

Numerical Simulations: The FEM simulations were performed with the COMSOL Multiphysics 5.3 software. The structures were first sketched using Autodesk Fusion 360 and then exported them into COMSOL Multiphysics. A linearly polarized plane wave with an excitation wavelength of 633 or 785 nm was incident directly upon the plasmonic nanostructures with polarization along the AuNP-nanopillar axis. In the simulations, the permittivity of Au was set to $\epsilon_{\text{Au}} = -12.101 + 1.2208i$ at 633 nm and $\epsilon_{\text{Au}} = -22.855 + 1.425i$ at 785 nm.^[38] The refractive indexes of PET and PFDT were taken as 1.630 and 1.333, respectively.^[39]

Supporting Information

Supporting Information is available from the Wiley Online Library or from the author.

Acknowledgements

This work was supported by the Fundamental Research Program (PNK 6070) of the Korean Institute of Materials Science (KIMS) and the Ministry of Trade, Industry and Energy (Grant N0002310). S.A.M. acknowledges ONR Global, the EPSRC Reactive Plasmonics Programme (EP/M013812/1), the Lee-Lucas Chair in Physics, and the Bavarian Solar Energies Go Hybrid (SolTech) programme. X.X. was supported by Lee Family Scholars. H.I. was supported in part by

National Cancer Institute of the National Institutional of Health under award number R00CA201248.

Conflict of Interest

The authors declare no conflict of interest.

Keywords

3D nanostructures, plasmonic biosensors, spherical metal nanoparticles, surface diffusion, surface energy

Received: May 27, 2019

Revised: July 19, 2019

Published online:

- [1] S. Mubeen, S. Zhang, N. Kim, S. Lee, S. Kramer, H. Xu, M. Moskovits, *Nano Lett.* **2012**, *12*, 2088.
- [2] A. Moreau, C. Ciraci, J. J. Mock, R. T. Hill, Q. Wang, B. J. Wiley, A. Chilkoti, D. R. Smith, *Nature* **2012**, *492*, 86.
- [3] D. Wang, W. Zhu, M. D. Best, J. P. Camden, K. B. Crozier, *Sci. Rep.* **2013**, *3*, 2867.
- [4] R. Chikkaraddy, B. de Nijs, F. Benz, S. J. Barrow, O. A. Scherman, E. Rosta, A. Demetriadou, P. Fox, O. Hess, J. J. Baumberg, *Nature* **2016**, *535*, 127.
- [5] X. Li, W. C. H. Choy, X. Ren, D. Zhang, H. Lu, *Adv. Funct. Mater.* **2014**, *24*, 3114.
- [6] E. Lee, Y. Xia, R. C. Ferrier, H. N. Kim, M. G. Gharbi, K. J. Stebe, R. D. Kamien, R. S. Composto, S. Yang, *Adv. Mater.* **2016**, *28*, 2731.
- [7] D. Chand, K. Shingeta, T. Truong, E. Lui, A. Mihi, M. Schulmerich, P. V. Braun, R. Bhargava, J. A. Rogers, *Nat. Commun.* **2011**, *2*, 479.
- [8] D. Paria, K. Roy, H. J. Singh, S. Kumar, S. Raghavan, A. Ghosh, A. Ghosh, *Adv. Mater.* **2015**, *27*, 1751.
- [9] T. Y. Jeon, D. J. Kim, S.-G. Park, S.-H. Kim, D.-H. Kim, *Nano Convergence* **2016**, *3*, 1.
- [10] T. Y. Jeon, H. C. Jeon, S. Y. Lee, T. S. Shim, J.-D. Kwon, S.-G. Park, S.-M. Yang, *Adv. Mater.* **2014**, *26*, 1422.
- [11] S. A. Camacho, R. G. Sobral-Filho, P. H. B. Aoki, C. J. L. Constantino, A. G. Brolo, *ACS Sens.* **2018**, *3*, 587.
- [12] K. Bantz, A. F. Meyer, N. J. Wittenberg, H. Im, O. Kurtulus, S. H. Lee, N. C. Lindquist, S. H. Oh, C. L. Haynes, *Phys. Chem. Chem. Phys.* **2011**, *13*, 11551.
- [13] H. Im, H. Shao, Y. I. Park, V. M. Peterson, C. M. Castro, R. Weissleder, H. Lee, *Nat. Biotechnol.* **2014**, *32*, 490.
- [14] A. P. Olson, K. B. Spies, A. C. Browning, P. A. G. Soneral, N. C. Lindquist, *Sci. Rep.* **2017**, *7*, 9135.
- [15] P. Christopher, H. Xin, A. Marimuthu, S. Linic, *Nat. Mater.* **2012**, *11*, 1044.
- [16] S. Linic, U. Aslam, C. Boerigter, M. Morabito, *Nat. Mater.* **2015**, *14*, 567.
- [17] U. Aslam, S. Chavez, S. Linic, *Nat. Nanotechnol.* **2017**, *12*, 1000.
- [18] S. Mubeen, J. Lee, N. Singh, S. Kramer, G. D. Stucky, M. Moskovits, *Nat. Nanotechnol.* **2013**, *8*, 247.
- [19] W. Hou, S. B. Cronin, *Adv. Funct. Mater.* **2013**, *23*, 1612.
- [20] S. A. Maier, *Plasmonics: Fundamentals and Applications*, Springer, New York, NY **2007**.
- [21] G. Yuan, E. T. F. Rogers, N. I. Zheludev, *Light: Sci. Appl.* **2019**, *8*, 2.
- [22] J. Ko, S. G. Park, S. Lee, X. Wang, C. Mun, S. Kim, D. H. Kim, J. Choo, *ACS Appl. Mater. Interfaces* **2018**, *10*, 6831.

- [23] S.-G. Park, C. Mun, X. Xiao, A. Braun, S. Kim, V. Giannini, S. A. Maier, D.-H. Kim, *Adv. Funct. Mater.* **2017**, *27*, 1703376.
- [24] M. Lee, T. Y. Jeon, C. Mun, J.-D. Kwon, J. Yun, S.-H. Kim, D.-H. Kim, S.-C. Chang, S.-G. Park, *RSC Adv.* **2017**, *7*, 17898.
- [25] X. Wang, S. G. Park, J. Ko, X. Xiao, V. Giannini, S. A. Maier, D. H. Kim, J. Choo, *Small* **2018**, *14*, 1801623.
- [26] C. J. Smithells, *Smithells Metals Reference Book* (Eds: W. F. Gale, T. C. Totemeier), Vol. 3, Butterworth-Heinemann, Oxford, UK **2004**, p. 11.
- [27] M. Grzelczak, A. Sanchez-Iglesias, H. Heidari, S. Bals, I. Pastoriza-Santos, J. Perez-Juste, L. M. Liz-Marzan, *ACS Omega* **2016**, *1*, 177.
- [28] M. Ohring, *Materials Science of Thin Films*, Academic Press, San Diego **2002**.
- [29] J. C. Love, L. A. E. Jennah, K. Kriebel, R. G. Nuzzo, G. M. Whitesides, *Chem. Rev.* **2005**, *105*, 1103.
- [30] C. T. Campbell, *Surf. Sci. Rep.* **1997**, *27*, 1.
- [31] F. Ruffino, G. Cacciato, M. G. Grimaldi, *J. Appl. Phys.* **2014**, *115*, 084304.
- [32] H. L. Skriver, N. M. Rosengaard, *Phys. Rev. B* **1992**, *46*, 7157.
- [33] A. H. Tavakoli, P. S. Maram, S. J. Widgeon, J. Rufner, K. van Benthem, S. Ushakov, S. Sen, A. Navrotsky, *J. Phys. Chem. C* **2013**, *117*, 17123.
- [34] A. Movsesyan, A. L. Baudrion, P. M. Adam, *Opt. Express* **2018**, *26*, 6439.
- [35] H. Shen, N. Guillot, J. Rouxel, M. Lamy de la Chapelle, T. Toury, *Opt. Express* **2012**, *20*, 21278.
- [36] S.-G. Park, M. Kang, S. Kim, H. S. Jung, D.-H. Kim, *Appl. Spectrosc. Rev.* **2018**, 1467440.
- [37] H. Im, Y. I. Park, D. Pathania, C. M. Castro, R. Weissleder, H. Lee, *Lab Chip* **2016**, *16*, 1340.
- [38] P. B. Johnson, R. W. Christy, *Phys. Rev. B* **1972**, *6*, 4370.
- [39] M. Kechadi, L. Chaal, V. Vivier, B. Tribollet, J. Gamby, *Phys. Chem. Chem. Phys.* **2016**, *18*, 20583.